Computer Methods in Applied Mechanics and Engineering 450 (2026) 118637

Contents lists available at ScienceDirect

Comput. Methods Appl. Mech. Engrg.

journal homepage: www.elsevier.com/locate/cma

Mechanics of complex network materials: A formulation based on phase field damage evolution on graphs

Marco Paggi

Scuola IMT Alti Studi Lucca, Piazza San Francesco 19, 55100 Lucca, Italy

ARTICLE INFO

Keywords:
Complex network materials
Phase field damage
Beam theory
Graphs
3D Printing polymers

ABSTRACT

A theory for simulating nonlocal damage in 2D lattice structures discretized by Euler-Bernoulli beam finite elements is herein proposed. A phase field approach to damage, projected onto the discretized nodes via the graph Laplacian matrix, is formulated to simulate damage evolution by solving a Helmholtz differential equation on the graph. Damage is introduced in the constitutive equations under the assumption of a bilateral damage evolution in tension and in compression, or a monolateral damage only in tension. Both formulations have been enhanced by a threshold driving force to better capture the onset of damage in polymers due to crazing. The staggered coupling scheme alternates between solving mechanical equilibrium and phase field equations, and it has been validated in relation to experiments on unnotched beams made of ABS subject to three-point bending. The approach is then applied to preliminary investigate the response of a complex network material in the nonlinear regime, contributing to understanding how graph-based topologies influence the load-bearing capacity of the material. The method bridges the gap between statistical physics of complex networks and nonlinear mechanics of materials and is expected to have an impact on the design of robust random metamaterials featuring nodes with large connectivities.

1. Introduction

Complex network materials are two- or three-dimensional lattices composed of randomly arranged vertices connected by edges. Unlike conventional lattice materials, where each vertex typically has a similar number of connecting edges, complex network materials exhibit a high degree of variability in connectivity. In particular, they feature *hubs*-nodes with significantly more connections than average (see the illustration in Fig. 1). This distinct topological characteristic sets complex network materials apart from traditional cellular or lattice structures [1–4], which have garnered substantial attention in the mechanics community for their wide-ranging applications in engineering and materials science. Borrowing terminology from chemistry, the vertices in complex network materials exhibit highly variable coordination numbers –that is, the number of neighboring vertices (analogous to atoms, ions, or molecules, known as ligands)– directly connected to a central vertex.

Complex network materials are commonly found in nature (Fig. 2), serving as key structural components of living cells and tissues. In certain cases, they can also be engineered to exhibit customized topologies. For example, Tang et al. [5] demonstrated that the topology of collagen-based biopolymer networks can change with temperature. Riedel et al. [6] successfully designed collagen matrices by inducing cross-linking through a reagent-free electron beam. Similarly, Hadjiargyrou [7] created various network matrices using electrospinning techniques.

E-mail address: marco.paggi@imtlucca.it

https://doi.org/10.1016/j.cma.2025.118637
Received 24 July 2025; Received in revised form 26 November 2025; Accepted 29 November 2025
Available online 5 December 2025

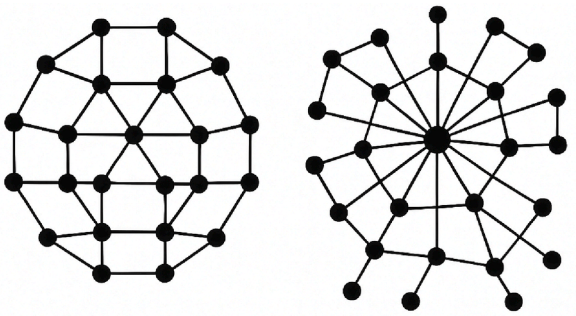

Fig. 1. Comparison between the topology of a conventional lattice material (left) and of a complex network material (right). The latter shows the appearance of hubs, i.e. vertices attracting a much larger number of connections.

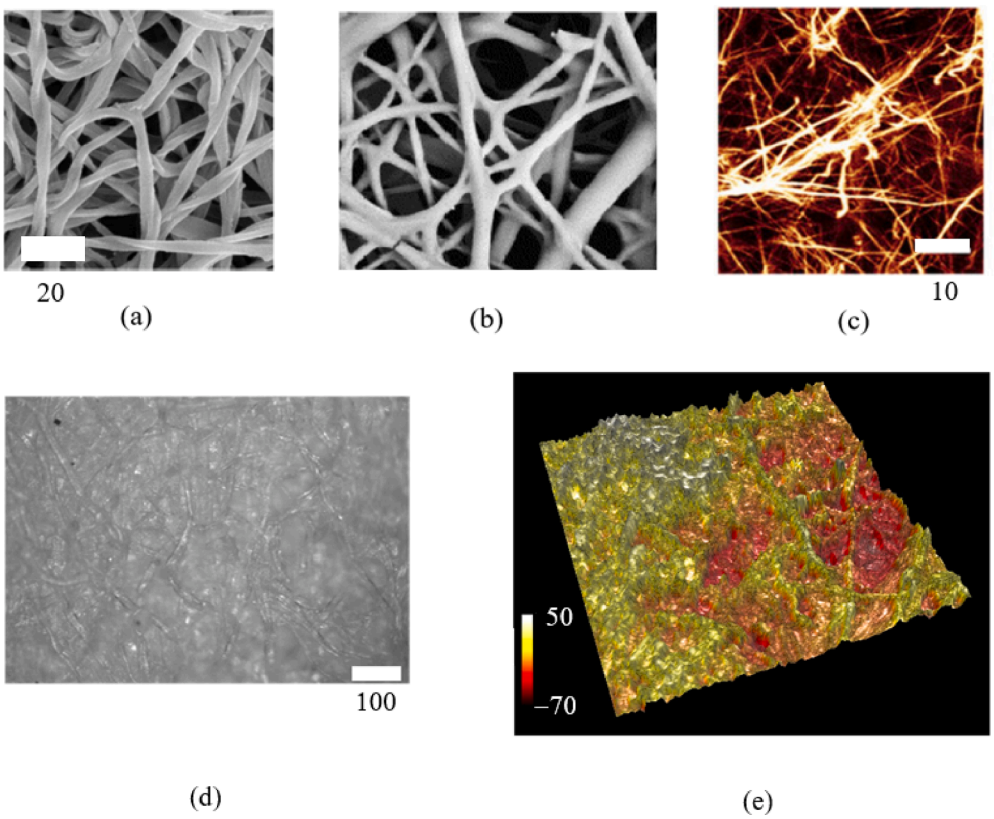

Fig. 2. (a) collagen network (adapted from [12], with permission); (b) fibers with size distribution from 375 nm to 1.1 μm in electrospun scaffolds (adapted from [7], CC 3.0); (c) electron irradiated collagen (adapted from [6], CC-BY); (d) paper morphology and (e) its surface topography showing the cellulose fibers. Scale bars are in micrometers.

Jaspers et al. [8] developed a series of hybrid polymers by combining semi-flexible ethylene glycol-functionalized polyisocyanides (PICs)-long polymers constrained in a relatively rigid helical conformation-with additional components such as stiff carbon nanotubes, networks of semi-flexible fibrin fibers, or flexible PAAm polymer networks.

Biological tissues also display intricate fiber arrangements embedded within a matrix [9]. From a technological perspective, another notable example includes cellulose fiber networks employed in the paper industry [10,11].

In all of those materials, cross-linking plays a crucial role for the mechanical response and substantially changes the response of the overall material from that of a single fiber [13]. The mechanical stability of such networks relies on the bending resistance of the fibers [14], in contrast to rubbers which are primarily governed by entropic stretching of polymer segments. Jansen et al. [12] identified the local coordination number (or connectivity) as a key architectural parameter that governs the elastic response of collagen. Sharma et al. [15] have shown a transition from a flexible to a rigid response of the network above a certain degree of connectivity, suggesting that the transition is strain-controlled. As an alternative explanation, the phenomenon of strain stiffening of filamentous protein networks was explored in [16] by means of a finite strain analysis of a two-dimensional network model of cross-linked semiflexible filaments, showing that the stiffening was caused by non-affine network rearrangements that govern a transition from a bending-dominated response at small strains to a stretching-dominated response at large strains.

Statistical physics have devised methods to reconstruct the geometry of biopolymer networks to synthetically investigate their mechanical response primarily in the elastic regime [17]. Shahsavari and Picu [18] proposed a computational model to study the effect on the material stiffness of adding fibers to a cross-linked network, again in the linear elastic regime, demonstrating that a superior stiffness can be achieved when a percolation-like threshold is overcome. van Doorn et al. [19] developed a theoretical approach by considering triangle networks and introducing cross-links into the model by assigning different mechanical properties to portions of triangles.

In parallel, the science of complex networks –spanning biological, social, and technological systems– has revolutionized over the past years the understanding of connectivity, robustness, and functionality of structured systems, exploiting computational and theoretical tools borrowed from graph theory, statistical physics and complex network science. The pioneering work in [20] has shown that the connection topology of networks is often assumed to be either completely regular or completely random, while many biological, technological and social networks lie somewhere in between these two extremes. Special attention has been devoted to finding scale-free networks, which are networks where fraction of vertices with a given number of connections (the so-called degree distribution) asymptotically follows a power law for very large values of connections [21,22]. While this is essential to describe the topology of social networks, whose graphs do have special vertices of very high degree called *hubs*, their role is also fundamental for the evolution of diffusive phenomena over the network itself. Notable examples regarded the spread of misinformation, the diffusion of infectious diseases, or even bank financial crises, see e.g. [23,24] and citations therein given.

Very recent contributions by Barabasi and his team [25–28] have further suggested to realize new materials inspired by graphs related to complex physical networks, potentially inspiring the design of new advanced metamaterials.

Drawing inspiration from these advances on network science and their prospective applications to materials enabled by 3D printing technologies [29], it is timely to establish computational methods hinging on structural mechanics theories to study their mechanical response and investigate their axial stretching and bending deformation also beyond the linear elastic response, and for polymeric materials used for 3D printing that often experience a progressive damage evolution due to crazing.

In this regard, the elements composing the edges can be reasonably well approximated by beam theory, and there is a wide literature for the simulation of damage and fracture in beams. Driven by research on quasi-brittle materials like concrete, nonlocal damage models have seen a wide development since the seminal paper in 1987 by Pijaudier-Cabot and Bažant [30]. The core principle of the method is to introduce an internal length scale into the material constitutive equations that regularizes the displacement field near damaging points that will lead to fracture. This regularization can be introduced in different ways. One possibility is to exploit an integral-type nonlocal formulation, where the damage at a point is determined by the weighted average of the strain field over a finite volume surrounding the point [31]. Alternatively, explicit or implicit gradient formulation have been proposed [32], where damage is driven not only by an equivalent strain in a point, but also by its Laplacian, which physically describes the spatial curvature of the strain distribution, multiplied by an internal length scale parameter. In the implicit version, a Helmoltz-type partial differential equation has to be solved to compute the regularized equivalent strain. As long as the strain distribution remains uniform (such as in a uniaxial tensile test before localization), the equivalent strain is also uniform, its Laplacian vanishes, and the model response is exactly the same as for the local formulation. After the onset of localization, the higher-order term is activated and prevents localization of damage in a set of zero measure. The reader is referred to [33–35] for a wider comparison among these formulations and computational aspects.

A more recent and powerful paradigm is the phase field approach to fracture [36,37]. This method, exploiting the Ambrosio-Tortorelli [38] functionals, provides a robust mathematical framework for modeling complex crack phenomena, including nucleation, propagation, branching, and merging, without the need to explicitly track the crack geometry [39–41]. It introduces a continuous auxiliary variable, the phase field, which smoothly transitions from a value of zero in the intact material to a value of one when the material is fully cracked. As for the nonlocal damage model, the phase field damage evolution equation assumes the form of a Helmoltz-type partial differential equation, and indeed the methodology shares several analogies with nonlocal damage mechanics formulated in its energy version [42]. The sharp discontinuity of a crack is thus approximated by a diffuse band, with its width controlled by a regularization parameter linked to the material's fracture properties. The evolution of this crack field is driven by the minimization of a global energy functional that balances stored elastic energy and the energy required to create new crack surface. The methodology has seen a rapid evolution for 2D and 3D continua since the fundamental work by Miehe [43], tackling the following major challenges: (*i*) introduction of different crack driving terms [44–46] to build damage only in tension, avoid material overlapping, and simulate structured deformations; (*ii*) acting on the crack density functional to simulate cohesive-type damage [47]; (*iii*) generalization to model elasto-plastic fracture [48–50]; (*iv*) implementation of the theory for structural elements, like shells [51,52] or beams [53,54] made of brittle materials.

The present work builds upon the previous formulations of the phase field approach to simulate nonlocal damage in Euler-Bernoulli beams [53,54], to establish a novel and efficient computational framework that directly connects the topological features of the complex beam network to its nonlinear mechanics response, thus enabling structural analysis of complex network materials.

This is done by introducing two specific new contributions. First, the evolution of the phase field variable is determined through the strong form of the differential problem instead of using the weak form. This leads to finite difference operators that generalize those stemming from the simulation of diffusive phenomena over a graph in the presence of the Helmoltz equation instead of the Laplacian equation. The operators describing damage evolution have now special features that are directly related to the network topology, and were not observable from the weak form. Second, having a single value of phase field attributed to a point along a beam requires making further assumptions to describe a material degradation that is also function of the point inside the beam cross-section. In this regard, a monolateral degradation of the elastic modulus in tension is proposed, with damage within the cross-section modelled as a step function (non-constant through the whole cross-section) between zero in compression and a value of damage

(from 0 to 1) given by the solution of the Helmoltz equation in the whole tensile region. This is considered to be more appropriate for polymeric materials subject to crazing than a sharp transition from zero to one as done in brittle materials [53]. Moreover, a simplified bilateral degradation, which renders the cross-sectional problem linear, is also examined. Both formulations are also enhanced by the introduction of a threshold value of the driving force for damage activation, which allows to better reproduce experimental results and, for the bilateral model, can be used to establish lower and upper approximations to the mechanical response. Finally, a preliminary case study related to the prototype experimental test on a complex network material produced by 3D printing and recently reported in [29] is examined, to show the potential of the proposed methods.

2. Phase field damage evolution equations: From a continuum to a graph

2.1. Continuum formulation

The phase field approach to nonlocal damage for a continuum, as for instance a specimen tested under uniaxial tension, is based on the following Helmoltz (or linear second order modified Poisson) differential equation [36,43]:

$$(\mathcal{H}+1)s - l_0^2 \frac{\mathrm{d}^2 s}{\mathrm{d}z^2} = \mathcal{H}, \tag{1}$$

where l_0 is the internal length scale of the model and $\mathcal{H}(z) = 2l_0\psi/\mathcal{G}_c$ is the driver for damage evolution, function of the fracture energy $\mathcal{G}_c$ and of the strain energy density $\psi(\epsilon)$, which in general is a function of the spatial coordinate z.

Rearranging Eq. (1) to a standard form and dividing it by $-l_0^2$ to make unity the coefficient of the highest derivative, one has:

$$\frac{\mathrm{d}^2 s}{\mathrm{d}z^2} - \frac{\mathcal{H}+1}{l_0^2} s = -\frac{\mathcal{H}}{l_0^2}. \tag{2}$$

Its complete solution is given by the sum of the solution of the corresponding homogeneous equation and its particular solution related to the form of the term on the right-hand-side. The homogeneous equation is:

$$\frac{\mathrm{d}^2 s_{\mathrm{hom}}}{\mathrm{d}z^2} - \frac{\mathcal{H}+1}{l_0^2} s_{\mathrm{hom}} = 0, \tag{3}$$

which, in the most general case, is a second-order linear ODE with non constant coefficients. If $\mathcal{H}(z) = \overline{\mathcal{H}} = \text{constant}$, then a closed-form expression can be easily derived through the characteristic equation:

$$r^2 - \frac{\overline{\mathcal{H}}+1}{l_0^2} = 0 \implies r = \pm\frac{\sqrt{\overline{\mathcal{H}}+1}}{l_0}, \tag{4}$$

and the general solution to the homogeneous equation becomes:

$$s_{\mathrm{hom}}(z) = A\exp\left(\frac{\sqrt{\overline{\mathcal{H}}+1}}{l_0} z\right) + B\exp\left(-\frac{\sqrt{\overline{\mathcal{H}}+1}}{l_0} z\right), \tag{5}$$

where A and B are constants determined by the imposition of the boundary conditions.

The particular solution is obtained by noting that the inhomogeneous term is a constant, so we can guess a constant particular solution $s_p = c$. Substituting into the inhomogeneous equation:

$$\frac{\mathrm{d}^2 s_p}{\mathrm{d}z^2} - \frac{\overline{\mathcal{H}}+1}{l_0^2} s_p = -\frac{\overline{\mathcal{H}}}{l_0^2} \implies 0 - \frac{\overline{\mathcal{H}}+1}{l_0^2} c = -\frac{\overline{\mathcal{H}}}{l_0^2}. \tag{6}$$

and solving for c, the particular solution reads:

$$s_p = \frac{\overline{\mathcal{H}}}{\overline{\mathcal{H}}+1}. \tag{7}$$

The general solution is therefore the sum of the homogeneous and particular solutions:

$$s(z) = s_{\mathrm{hom}}(z) + s_p = A\exp\left(\frac{\sqrt{\overline{\mathcal{H}}+1}}{l_0} z\right) + B\exp\left(-\frac{\sqrt{\overline{\mathcal{H}}+1}}{l_0} z\right) + \frac{\overline{\mathcal{H}}}{\overline{\mathcal{H}}+1}. \tag{8}$$

For $\overline{\mathcal{H}} = 0$ and imposing $s(z=0) = 1$ and $s(z\to\infty) = 0$, one obtains the well-known solution $s = \exp(-|z|/l_0)$, which corresponds to an exponential decay of damage from the point where fracture localizes ($s = 1$) to zero at infinity.

2.2. Projection on a graph

To project the above differential equation on a discrete system made of vertices connected by edges, we exploit the graph Laplacian matrix.

In a graph $\mathcal{G} = (\mathcal{V}, \mathcal{E})$, with $\mathcal{V}$ vertices connected by $\mathcal{E}$ edges, where the vertices are discrete points where s has to be computed and edges represent connections between nodes over which damage diffuses, the graph Laplacian matrix $\boldsymbol{\mathcal{L}}$ encodes the physics of

the diffusion process graph-specific in terms of its unique topology. The graph Laplacian matrix operator is defined as the following difference [55]:

$$\boldsymbol{\mathcal{L}} = \boldsymbol{\mathcal{D}} - \boldsymbol{\mathcal{A}}, \tag{9}$$

where $\boldsymbol{\mathcal{A}}$ is the symmetric adjacency matrix and $\boldsymbol{\mathcal{D}}$ is the diagonal degree matrix. The adjacency matrix $\boldsymbol{\mathcal{A}}$ of a graph assembles its edge weights into a matrix whose entries are:

$$\mathcal{A}_{ij} = \begin{cases} w_{ij}, & \text{if} \quad \{\mathcal{V}_i, \mathcal{V}_j\} \in \mathcal{E}_{ij}, \\ 0, & \text{if} \quad \{\mathcal{V}_i, \mathcal{V}_j\} \notin \mathcal{E}_{ij}, \end{cases} \tag{10}$$

where w_{ij} is the weight associated to the edge (i, j).

The diagonal degree matrix $\boldsymbol{\mathcal{D}}$ of the graph lists the degree of node i on the diagonal entry $\boldsymbol{\mathcal{D}}_{ii}$ and, for an undirected weighted graph, it is defined as:

$$\mathcal{D}_{ii} = \sum_{j=1}^{n} \mathcal{A}_{ij}, \tag{11}$$

where n is the total number of vertices. If all the edges have the same weight $w_{ij} = 1$, then $\mathcal{D}_{ii}$ is simply equal to the number of neighboring vertices j connected to i by an edge $\mathcal{E}_{ij}$.

In the most general case of a weighted graph where edges contribute to damage diffusion with different weights $w_{i,j}$, one has:

$$\mathcal{L}_{ij} = \begin{cases} -w_{ij} & \text{if } i \neq j, \\ \sum_{k \neq i} w_{ik} & \text{if } i = j, \ k = 1, \dots, n \\ 0 & \text{otherwise.} \end{cases} \tag{12}$$

Based on this operator, the continuous Laplacian $\nabla^2 s$ becomes the graph Laplacian applied to s through this transformation:

$$\nabla^2 s \quad \rightarrow \quad -\boldsymbol{\mathcal{L}}\, \mathbf{s}, \tag{13}$$

where $\mathbf{s} = [s_1, s_2, \dots, s_n]^T$ is the vector of unknown damage values at vertices.

Therefore, the discrete version of the differential problem is obtained by replacing the continuous terms with the discrete ones:

$$\boldsymbol{\mathcal{H}}^m \mathbf{s} + l_0^2 \boldsymbol{\mathcal{L}}\, \mathbf{s} = \boldsymbol{\mathcal{H}}^v \tag{14}$$

where $\mathcal{H}_i^v = \mathcal{H}_i$ $(i = 1, \dots, n)$ and:

$$\boldsymbol{\mathcal{H}}_{ij}^m = \begin{cases} 1 + \mathcal{H}_i & \text{if} \quad i = j, \\ 0 & \text{if} \quad i \neq j. \end{cases} \tag{15}$$

The solution of the obtained algebraic set of equations is:

$$\mathbf{s} = \left[\boldsymbol{\mathcal{H}}^m + l_0^2 \boldsymbol{\mathcal{L}}\right]^{-1} \boldsymbol{\mathcal{H}}^v \tag{16}$$

along with imposed boundary conditions. Due to the sparsity of the operators involved, this can be efficiently achieved using solvers designed for sparse matrices and parallel computations.

A physical interpretation of the formulation can be given by noting that the term $\boldsymbol{\mathcal{H}}^m$ corresponds to a local reaction (e.g., source/sink at each node), the term $l_0^2 \boldsymbol{\mathcal{L}}\, \mathbf{s}$ represents diffusion over the graph edges, and the right-hand side $\boldsymbol{\mathcal{H}}^v$ is a forcing term.

Remark: it is possible to show that the discretized form of the phase field damage evolution on a graph leads to an approximation of the continuous solution $s = \exp(-|z|/l)$ if $\mathcal{H} = \overline{\mathcal{H}}$ is a constant. Let's consider a graph of n vertices distributed over a straight line from $z = 0$ to $z = z_{\max}$, with edges connecting a vertex to the two adjacent ones, except from the first and the last that are connected to a single edge.

The matrix form of the full system reads:

$$\begin{bmatrix} 1+\overline{\mathcal{H}} & 0 & \dots & \dots & 0 \\ 0 & 1+\overline{\mathcal{H}} & 0 & \dots & 0 \\ \dots & \dots & \dots & \dots & \dots \\ 0 & \dots & 0 & 1+\overline{\mathcal{H}} & 0 \\ 0 & \dots & \dots & 0 & 1+\overline{\mathcal{H}} \end{bmatrix} \begin{bmatrix} s_1 \\ \vdots \\ \vdots \\ \vdots \\ s_n \end{bmatrix} + l_0^2 \begin{bmatrix} a/2 & b & 0 & \dots & \dots & 0 \\ b & a & b & 0 & \dots & 0 \\ \dots & \dots & \dots & \dots & \dots & \dots \\ 0 & \dots & 0 & b & a & b \\ 0 & \dots & \dots & 0 & b & a/2 \end{bmatrix} \begin{bmatrix} s_1 \\ \vdots \\ \vdots \\ \vdots \\ s_n \end{bmatrix} = \begin{bmatrix} \overline{\mathcal{H}} \\ \vdots \\ \vdots \\ \vdots \\ \overline{\mathcal{H}} \end{bmatrix}, \tag{17}$$

where $a = 2w$, $b = -w$. If the weight w associated to the links is set equal to the inverse of the square of each edge length, $w = 1/h_e^2 = [(n-1)/z_{\max}]^2$, then the graph Laplacian matrix reduces to a finite difference operator. Boundary conditions, in analogy with those of

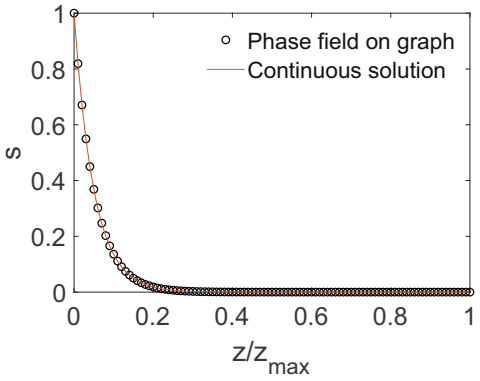

Fig. 3. Comparison between the numerical solution based on the phase field projected on a graph and its exact continuous analytical solution for the monodimensional benchmark problem.

the continuous problem, are $s(0) = 1$ and $s(z_{\max}) = 0$ and their imposition requires partitioning the set of equations by retaining only the nodes from 2 to $n-1$ where damage is unknown. The modified set of equations after imposing the boundary conditions reads:

$$\mathbf{s} = \left[\boldsymbol{\mathcal{H}}^{m*} + l_0^2 \boldsymbol{\mathcal{L}}^*\right]^{-1} \left(\boldsymbol{\mathcal{H}}^{v*} - \mathbf{f}\right), \tag{18}$$

where $\mathbf{s}^* = [s_2, \dots, s_{n-1}]$, $\boldsymbol{\mathcal{H}}^{m*}$ is a diagonal matrix of size $(n-2)\times(n-2)$ restricted to the corresponding nodal unknowns, $\boldsymbol{\mathcal{H}}^{v*}$ is a vector of size $(n-2)\times 1$, $\boldsymbol{\mathcal{L}}^*$ is the submatrix obtained from $\boldsymbol{\mathcal{L}}$ as $\boldsymbol{\mathcal{L}}_{ij}$ with $i, j = 2, \dots, n-1$, and $\mathbf{f} = [l_0^2 s_1, 0, \dots, 0, l_0^2 s_n]^T$ accounts for the boundary conditions.

If the forcing term is zero, $\overline{\mathcal{H}} = 0$, then the solution reduces to:

$$\mathbf{s}^* = -\left[\mathbf{I}^* + l_0^2 \boldsymbol{\mathcal{L}}^*\right]^{-1} \mathbf{f}, \tag{19}$$

where $\mathbf{I}^*$ is a $(n-2)\times(n-2)$ identity matrix.

The discrete approximation is compared in Fig. 3 with the analytical solution for the continuous phase field problem determined in Section 2.1, setting $z_{\max} = 10$ m, $l_0/z_{\max} = 0.05$, and $n = 101$, shoving that the approximated solution and the exact analytical one for a continuum are coincident.

3. Coupling phase field evolution with mechanics of an Euler-Bernoulli beam

3.1. Mathematical formulation

The strong form of the coupled problem consisting in the elastic equilibrium field equations and the phase field damage evolution equation reads:

$$\nabla \cdot \boldsymbol{\sigma} = \mathbf{f}_v, \tag{20a}$$

$$(\mathcal{H} + 1)s - l_0^2 \frac{\mathrm{d}^2 s}{\mathrm{d}z^2} = \mathcal{H}, \tag{20b}$$

where $\boldsymbol{\sigma}$ is the stress tensor and $\mathbf{f}_v$ is the vector accounting for volumetric forces, to be complemented by Dirichlet and Neumann boundary conditions as customary. Here, z is considered to be the axial (curvilinear) coordinate of each straight edge. The two differential problems in Eq. (20) are coupled by the fact that damage affects the stress components through the damaged constitutive matrix that relates the stress tensor to the strain tensor and, in turn, the stress components enter the driving parameter $\mathcal{H}$ through the strain energy.

When projected onto a graph representing a network material, it is convenient to write the elastic equations in a weak form. The strong differential form of the phase field equation has also to be replaced by its projection on a graph, Eq. (14):

$$\int_{\mathcal{E}} \int_{\Omega_e} \boldsymbol{\sigma}^T \, \delta\boldsymbol{\epsilon} \, \mathrm{d}\Omega \, \mathrm{d}\mathcal{E} = \int_{\mathcal{E}} \int_{\Omega_e} \mathbf{f}_v \, \delta\mathbf{u} \, \mathrm{d}\Omega \, \mathrm{d}\mathcal{E}, \tag{21a}$$

$$\boldsymbol{\mathcal{H}}^m \mathbf{s} + l^2 \boldsymbol{\mathcal{L}} \, \mathbf{s} = \boldsymbol{\mathcal{H}}^v. \tag{21b}$$

where the above integral over the volume has been split into an integral over the edge cross-section, Ω_e, and an integral over the curvilinear axis of the structure, $\mathcal{E}$.

From the numerical point of view, the complex network material, whose structure is encoded into its graph composed by edges connecting vertices, can be modeled as a frame discretized by beam finite elements, assigning geometrical properties to the edge cross-sections Ω_e and material properties related to the material composition, function also of damage whose value can vary along the beam longitudinal axis.

It is important to remark that, as a major difference from the Laplacian partial differential equation of the type $\nabla s = Q$ widely used in physics of complex networks to simulate diffusion on a graph (spread of misinformation, etc.), here we have to comply with the internal length scale l_0 of the phase field approach. This requires introducing a discretization of edges into beam elements of size $h_e \leq l_0/2$. This is accomplished upon defining l_0 and a given user-defined h_e/l_0 ratio, and discretizing each edge by ceil(L_e/h_e) beam elements, where L_e is the beam span. As a result, the data structure will consist of a series of additional computational nodes inserted between vertices, equi-spaced by the distance h_e.

The internal stress state can be further expressed through the characteristics of internal reactions of beams, which are computed as the integral of the stress field components over Ω_e. Introducing a reference frame where x and y are the coordinates in the plane of the cross-section and z is the longitudinal coordinate, for 2D frames we have to consider the axial force N, the bending moment M_x with respect to the x-axis, and the shearing force T_y with respect to the y-axis. Such internal forces make work with their dual virtual generalized displacements $\delta\epsilon_0$ (virtual axial strain), $\delta\chi_x$ (virtual curvature with respect to the x-axis), and $\delta\gamma_y$ (virtual shear deformation with respect to the y-axis). Hence, the weak form associated to the mechanical field reads:

$$\int_{\mathcal{E}} (N\delta\epsilon_z + M_x\delta\chi_x + T_y\delta\gamma_y)\,\mathrm{d}\mathcal{E} = L_{\text{ext}}, \tag{22a}$$

$$\boldsymbol{\mathcal{H}}^m\,\mathbf{s} + l_0^2\boldsymbol{\mathcal{L}}\,\mathbf{s} = \boldsymbol{\mathcal{H}}^v, \tag{22b}$$

where L_{ext} is the virtual work done by the external forces.

The introduction of the finite element discretization based on Euler-Bernoulli beam finite elements [56][Ch. 5.4] leads to the following matrix form in the global reference system uniquely defined for all the beams:

$$\mathbf{K}\mathbf{U} = \mathbf{F}, \tag{23a}$$

$$\boldsymbol{\mathcal{H}}^m\,\mathbf{s} + l_0^2\boldsymbol{\mathcal{L}}\,\mathbf{s} = \boldsymbol{\mathcal{H}}^v, \tag{23b}$$

where $\mathbf{U} = \mathbb{A}(\mathbf{U}_e)$, $\mathbf{F} = \mathbb{A}(\mathbf{F}_e)$, and $\mathbf{K} = \mathbb{A}(\mathbf{K}_e)$ are the operators obtained from assembling the individual element contributions. Each of those terms is calculated by the multiplication with a matrix $\mathbf{r}_e$ that considers the rotation from the local reference frame aligned with the beam axis z to the global reference frame:

$$\mathbf{U}_e = \mathbf{r}_e\mathbf{U}_e^*, \tag{24a}$$

$$\mathbf{F}_e = \mathbf{r}_e\mathbf{F}_e^*, \tag{24b}$$

$$\mathbf{K}_e = \mathbf{r}_e'\mathbf{K}_e^*\mathbf{r}_e, \tag{24c}$$

where the rotation matrix $\mathbf{r}_e$ is calculated from the angle of inclination β_e of the longitudinal axis of the element from the global horizontal axis:

$$\mathbf{r}_e = \begin{bmatrix} \cos(\beta_e) & \sin(\beta_e) & 0 & 0 & 0 & 0 \\ -\sin(\beta_e) & \cos(\beta_e) & 0 & 0 & 0 & 0 \\ 0 & 0 & 1 & 0 & 0 & 0 \\ 0 & 0 & 0 & \cos(\beta_e) & \sin(\beta_e) & 0 \\ 0 & 0 & 0 & -\sin(\beta_e) & \cos(\beta_e) & 0 \\ 0 & 0 & 0 & 0 & 0 & 1 \end{bmatrix}. \tag{25}$$

The generalized displacement vector at the element level is defined as $\mathbf{U}_e^* = (u_1, v_1, \phi_{y1}, u_2, v_2, \phi_{y2})^T$, where 1 and 2 refer to the extremal nodes of the beam element. In absence of loads applied to the internal edges of the network material, the local internal force vector at the element level reads $\mathbf{F}_e = (N_1, T_{y,1}, M_{x,1}, N_2, T_{y,2}, M_{x,2})^T$.

Here, it has to be remarked that, while the algebraic set of equations related to the elastic Eqs. (23a) stem from the weak form of the original differential problem, the algebraic equations related to the phase field evolution (23b) have been derived from the discretization of the corresponding strong form. In both cases, the equations are now discretized and projected at nodes. This choice differs from what proposed in [53] or in [54], where the phase field equations have been treated using their conventional weak form which however does not allow to explicitly identify the connection with the topological operators of the underlying network.

3.2. Coupling strategies

The coupling of the elastic equilibrium equations with those describing phase field damage evolution introduces a dependency of the element stiffness matrix $\mathbf{K}_e$ upon the damage variable $s \in [0, 1]$ associated to any point inside the beam element. Viceversa, the term $\mathcal{H}$ entering the phase field evolution equations is connected to the elastic energy density ψ of the mechanical system, which is the driving parameter for damage evolution.

A monolithic treatment of the two differential problems would lead to a nonlinear problem that has been formulated and solved with a rigorous full Newton-Raphson incremental-iterative algorithm [52] for solid shells. Alternatively, a staggered (sequential) solution scheme can be devised (see the detailed analysis in [40,48]) which has also the significant advantage to allow using the standard solvers available for each individual differential problem. As discussed in [57], the use of a staggered scheme allows also to circumvent the loss of convexity that may occur in the monolithic form, facilitating the convergence of standard solvers. Hence, a staggered solution strategy is herein adopted, which means that each differential problem is solved in its primary unknown by freezing the unknown of the other problem taken from the previous iteration, and iterating between the two differential problems

until convergence in the quadratic norm of the damage variable s from two subsequent iterations. Therefore, in the iterative loop, the mechanical problem is solved for a fixed value of s, say $\bar{s}$.

In the most general situation, the phase field damage for a beam subject to an axial force and a bending moment is a function of the position along the beam axis, z, and on the coordinate y in the plane of bending $y-z$, while it is almost constant along the direction x. Very recently, a mixed FE formulation based on Euler-Bernoulli beams and a 2D continuum discretization for the weak form associated to the phase field problem for a brittle material has been proposed in [54]. While this approach certainly represents the most accurate way to approximate a 2D continuum simulation, it retains the complexity of solving the weak form of the phase field equations as a 2D continuum partial differential equation. The reduction of the field $s(x,y)$ to a single scalar value was attempted in [53], augmenting such a single scalar by introducing two ansatz variables that allow the simulation of a crack penetrating the cross-section, under the assumption that the phase field is either zero (pristine material) or unity (fractured material) along y. From the material viewpoint, while this approach is suitable to model a brittle material and it provides a fairly good approximation of full 2D solutions, it is less applicable to polymeric materials. Such materials in fact display large process zone sizes caused by crazing [58], with a resulting smoother progression of damage that is far from being sharp as for brittle materials [59,60].

Therefore, keeping in mind that reducing a field $s(x,y)$ to a single scalar value has to be done with care, two different possibilities are herein explored specifically with the aim of modelling damage evolution in materials like polymers used for 3D printing and subject to crazing, that represent a relevant enabling technology for the engineering realization of artificial network materials.

3.2.1. Bilateral degradation

In this instance, the scalar phase field variable $s = s(z)$ computed in the point z is used to degrade the Young's modulus of the material both in tension and in compression, regardless of x and y. In the staggered iteration we thus have:

$$E_s = E_0[(1-\bar{s})^2 + k_r], \tag{26}$$

where E_0 is the undamaged elastic modulus and k_r is a residual stiffness to avoid ill-conditioning of the system matrix. Such a choice, for a given $\bar{s}$, leads to a linear set of algebraic equations associated to the mechanical problem. Assuming that the cross-section remains planar after deformation, which is a common assumption in case of phase field damage [53,54], at the cross-section level the equilibrium equations

$$\int_\Omega \sigma_z \, \mathrm{d}\Omega = N, \tag{27a}$$

$$\int_\Omega \sigma_z \, y \, \mathrm{d}\Omega = M_x, \tag{27b}$$

become linear:

$$\int_\Omega E_s(\epsilon_0 + \chi_x y) \, \mathrm{d}\Omega = N, \tag{28a}$$

$$\int_\Omega E_s(\epsilon_0 + \chi_x y) \, y \, \mathrm{d}\Omega = M_x, \tag{28b}$$

since E_s is constant in the staggered iteration, and provide ϵ_0 and χ_x as a function of N and M_x. Therefore, the position of the neutral axis depends solely on N and M_x, and not on $\bar{s}$.

The driving parameter $\mathcal{H}$ for the phase field equations is then computed as:

$$\mathcal{H} = \frac{2G_c\psi}{l_0} = \frac{G_c}{l_0}\left(N\epsilon_0 + M_x\chi_x\right) \tag{29}$$

3.2.2. Monolateral degradation

In this case, damage is activated only within the portion of the cross-section subject to a tensile axial stress, while the material in compression is kept undamaged. This implies the use of a damage function s dependent not only on z but also on y, which takes 0 for the cross-sectional points above (below) the neutral axis and $\bar{s}$ for the points below (above) it, for a positive (negative) bending moment:

$$E_s = \begin{cases} E_0, & \text{for } \epsilon_z \le 0 \\ E_0[(1-\bar{s})^2 + k_r], & \text{for } \epsilon_z > 0 \end{cases} \tag{30}$$

The mechanical problem becomes nonlinear and it mathematically corresponds to finding the equilibrated internal reactions and the related compatible axial strain for a bi-material beam whose portion in compression maintains the elastic modulus E_0 and is fully bonded to the portion in tension whose elastic modulus E_s has been degraded by the damage variable $\bar{s}$. The neutral axis separates the two portions and its position $\bar{y}$ is an unknown that depends on $\bar{s}$ and on the characteristics of internal reaction, N and M_x, which in turn depend upon the generalized solution of the elastic problem, $\mathbf{U}$.

Again, under the assumption of planarity of the beam cross-section, one has to find $\bar{y}$, ϵ_0, and χ_x from the two equilibrium Eqs. (28), for given N and M_x, in addition to the formula providing the neutral axis position, $\bar{y} = -\epsilon_0/\chi_x$. This set of three nonlinear algebraic equations has to be solved iteratively.

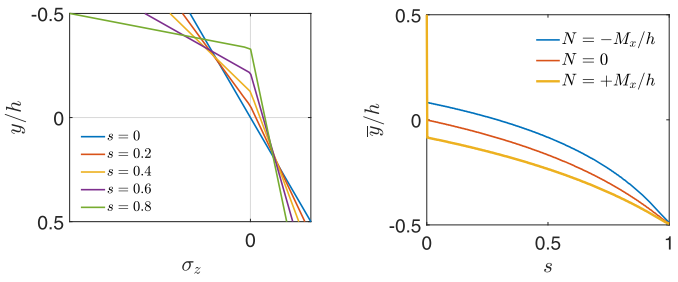

(a) Axial stress distribution ($N = 0$)

(b) Neutral axis position vs. damage

Fig. 4. Evolution of the neutral axis position when the elastic modulus is damaged only in tension ($\sigma_z > 0$), for a given damage s and applied bending moment $M_x > 0$ and axial force N. The positive M_x is tensioning the cross-section at its intrados ($y = h/2$).

After some algebraic manipulation, the above three governing equations for $\bar{y}$, ϵ_0, and χ_x can be reduced to a single nonlinear implicit equation in terms of $\bar{y}(\bar{s})$:

$$(M_{22} - M_{12}\,\bar{y})N - (M_{12} - M_{11}\bar{y})M_x = 0, \tag{31}$$

whose terms are:

$$M_{11} = \int_{\Omega_e} E_s \,\mathrm{d}\Omega, \tag{32a}$$

$$M_{12} = \int_{\Omega_e} E_s\, y \,\mathrm{d}\Omega, \tag{32b}$$

$$M_{22} = \int_{\Omega_e} E_s\, y^2 \,\mathrm{d}\Omega. \tag{32c}$$

For a rectangular cross-section of base b and height h, the following closed-form expressions apply:

$$M_{11} = \left\{A_0\, E_0 + A_s\, [(1-\bar{s})^2 + k_r]\right\}, \tag{33a}$$

$$M_{12} = \left\{S_x^{A_0}\, E_0 + S_x^{A_s}\, [(1-\bar{s})^2 + k_r]\right\}, \tag{33b}$$

$$M_{22} = \left\{I_x^{A_0} E_0 + I_x^{A_s} [(1-\bar{s})^2 + k_r]\right\}, \tag{33c}$$

$$A_0 = \left(\frac{h}{2} + \bar{y}\right)b, \tag{33d}$$

$$A_s = bh - A_0, \tag{33e}$$

$$S_x^{A_0} = -S_x^{A_s} = -\left(\frac{h^2}{4} - \bar{y}^2\right)\frac{b}{2}, \tag{33f}$$

$$I_x^{A_0} = b\left(\frac{h}{2} + \bar{y}\right)\left(\frac{h}{4} - \frac{\bar{y}}{2}\right)^2 + \frac{b}{12}\left(\frac{h}{2} + \bar{y}\right)^3, \tag{33g}$$

$$I_x^{A_s} = \frac{bh^3}{12} - I_x^{A_0}, \tag{33h}$$

where the nonlinearity of Eq. (31) becomes evident due to the dependency of the terms in Eq. (33) upon $\bar{y}$.

Once $\bar{y}$ is found using a standard Netwon-Raphson solver to linearize the nonlinear equation, the set of algebraic Eqs. (28) is solved to compute the converged values of ϵ_0 and χ_x, which again allow to quantify the driving parameter $\mathcal{H}$ for the phase field equations as in (29).

To visualize the effect of damage on the internal stress state in the mono-lateral degradation model, an exemplary problem (rectangular cross-section with $b = 0.2$ m, $h = 0.4$ m, variable N, $M_x = 1 \times 10^7$ Nm, $E_0 = 30$ GPa, $k_r = 0.0001$) is simulated. The axial stress distributions $\sigma_z(y)$ are shown in Fig. 4a for 6 increasing values of s. For $s = 0$, the stress field (blue curve) has a neutral axis $\bar{y} = 0$ and is anti-symmetric as for a homogeneous beam, with the portion of the cross-section in tension at the intrados ($M_x > 0$). By increasing the value of damage s, the neutral axis progressively moves towards the extrados, up to $y = -h/2$, to balance the reduced contribution of the damaged material for $y > \bar{y}$ (which has a damaged elastic modulus E_s), and guarantee the equilibrium with the internal reactions. The position of the neutral axis $\bar{y}$ vs. s is shown in Fig. 4b for $N = 0$ (orange curve), and also for a positive (yellow) and a negative (blue) axial force N. Negative valued N induce a superimposed compressive stress state that increases the value of $\bar{y}$ with respect to the other cases, for the same applied s. When $\bar{y}/h \to -0.5$, the cross-section becomes a hinge with a residual stiffness k_r.

3.2.3. Technical comparison between different degradation assumptions and introduction of a threshold for damage nucleation

The above degradation assumptions reduce the dependency of the damage variable $s(y, z)$ to a constant in case of bilateral degradation, or to a step-wise function of y for the monolateral degradation. In both cases, the damage field can have any intermediate value between 0 and 1 within the cross-section, which is deemed to be suitable to describe aprogressive material degradation of

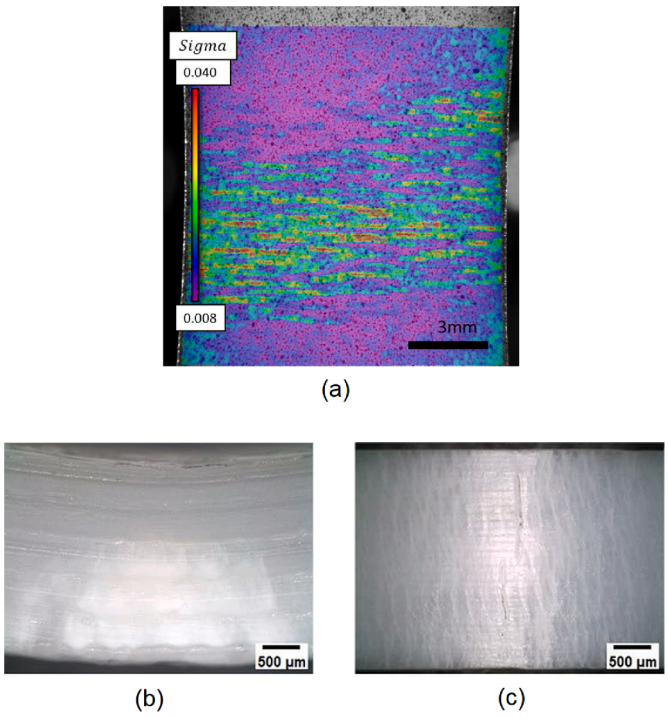

Fig. 5. Development of crazing observed through red color via digital image correlation in tensile tests on compressed molded ABS (a) (adapted from [59]); development of crazing (white zones) in 3D printed three-point bending tests: lateral view (b) and bird view of the intrados in tension (c) (adapted from [60]). (For interpretation of the references to colour in this figure legend, the reader is referred to the web version of this article).

polymers subject to crazing. This constitutes a major difference from existing phase field models for beams [53,54] conceived for LEFM of brittle materials, which lead to $s = 0$ or 1 along the cross-section depth, as for a through-depth sharp crack.

As a technical case-study to assess the potential and the limitations of the present approach, let's consider an unnotched beam made of ABS and subject to three-point bending as experimentally tested in [61]. The beam had a span $L = 50.8$ mm and constant rectangular cross-section with base $b = 3.18$ mm and height $h = 12.7$ mm, hinged at $z = 0$ and simply supported at $z = L$, subject to a vertical concentrated force F in the mid-span position. The Young's modulus of ABS had been reported equal to $E_0 = 1826$ MPa. In the numerical simulations, the beam has been discretized into $n = 301$ nodes, with $k_r = 0.001$, $G_c = 0.2$ Nm$^{3/2}$, and $l_0 = 4$ mm. While no measurements on G_c were available from [61] and that model parameter should be considered as a dissipation energy associated to crazing rather than to brittle fracture, the internal length scale l_0 has been set to be consistent with the wide spread of crazing in bending as experimentally reported in [59,61], see the images and the scale bars in Fig. 5.

Since the beam is isostatic, the solution of the static problem under force control gives the characteristics of internal reactions at any z, which are independent of the beam deformability and on s:

$$N = 0, \tag{34a}$$

$$M_x(z) = \begin{cases} Fz/2, & 0 \le z \le L/2, \\ F(L-z)/2, & L/2 \le z \le L, \end{cases} \tag{34b}$$

$$T_y(z) = \begin{cases} F/2, & 0 \le z \le L/2, \\ -F/2, & L/2 \le z \le L. \end{cases} \tag{34c}$$

Neglecting the effect of shear deformability according to the Euler-Bernoulli beam theory, the only relevant internal force component for this benchamrk test is M_x.

The force vs. mid-span deflection curves predicted by the models under force control based on a monolateral or a bilateral damage evolution is shown in Fig. 6a, along with the experimental results from [61] (dots) and the linear elastic material response (dashed line) as a reference baseline in absence of damage. Both models tend to overestimate the evolution of damage progression, which takes place very soon, driven by $\psi(z)$, while experiments show that the departure from the linear elastic regime takes place for $F > 80$ N. Moreover, as expected, monolateral damage evolution is more gradual than the bilateral one, see Fig. 6b for the same set of input parameters and Fig. 6c along the beam for different loadlevels (dashed curves: monolateral damage model; solid curves bilateral

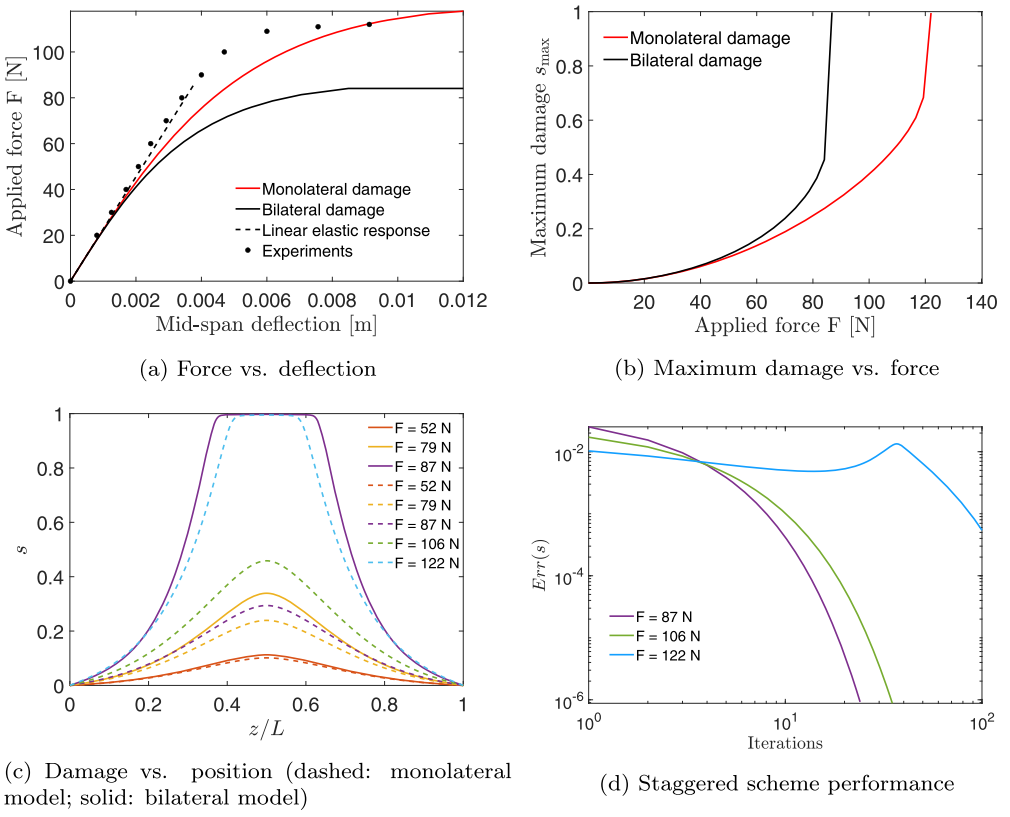

(a) Force vs. deflection

(b) Maximum damage vs. force

(c) Damage vs. position (dashed: monolateral model; solid: bilateral model)

(d) Staggered scheme performance

Fig. 6. Model predictions for a three-point bending isostatic beam. Experiments from [61].

damage model). The convergence of the staggered scheme is similar in the two models in terms of number of iterations, but of course the bilateral model is much faster since the elastic problem is linear and does not require a nested iterative solution scheme. The L_2 norm of the relative error on the phase field variable s is shown in Fig. 6d for the monolateral degradation model and goes down to 1×10^{-6} when $s < 1$, while it does not converge when $s \to 1$ and the structure loses its elastic equilibrium due to the formation of a kinematism.

To improve the model predictions and avoid damage accumulation from the onset of deformation, which is not consistent with the actual evolution of the stiffness degradation measured in the experiments, a threshold value $\mathcal{H}_c$ to the driving force term is herein introduced. Therefore, in the enhanced formulation, the actual driving force $\mathcal{H}$ is computed as:

$$\mathcal{H} = \begin{cases} 0, & \mathcal{H} \leq \mathcal{H}_c \\ \mathcal{H}, & \mathcal{H} > \mathcal{H}_c \end{cases} \tag{35}$$

Setting $\mathcal{H}_c = 0.3$ (N/m)^2, we obtain the monolateral damage model predictions in Fig. 7 (red solid line), which are a better approximation of the experimental trend. Acting on the value of $\mathcal{H}_c$, the bilateral damage model can also provide a technical approximation of the monolateral one, as shown in Fig. 7, where the lower approximation (in black) has been obtained by setting $\mathcal{H}_c = 0.3$ (N/m)^2, and the upper approximation (in blue) corresponds to $\mathcal{H}_c = 0.75$ (N/m)^2. Therefore, although the bilateral damage model leads to a sharper dynamical evolution of damage towards unity, it may still be an option to be considered as a compromise between accuracy and reduction of computational costs, since the reduced mechanical problem becomes linear.

3.3. Finite element implementation

In the FE procedure, the phase field variable along z is obtained via a linear interpolation between the elemental nodal values s_1 and s_2:

$$s = N_1(z)s_1 + N_2(z)s_2, \tag{36}$$

where $N_1 = (1 - z/h_e)$, $N_2 = z/h_e$, $z \in [0, h_e]$, being h_e the finite element size.

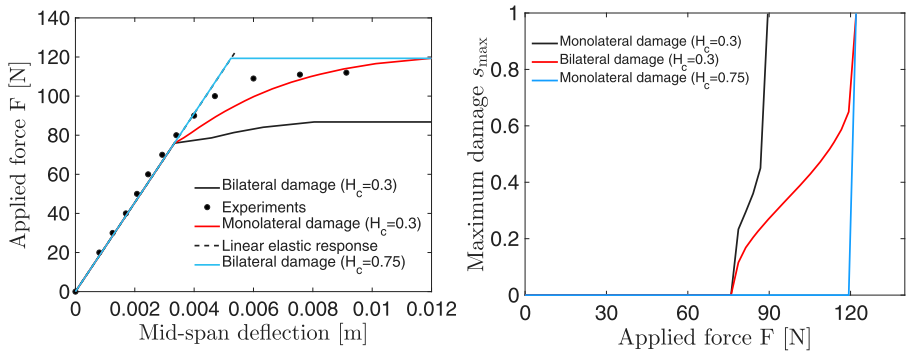

(a) Force vs. deflection

(b) Maximum damage vs. force

Fig. 7. Model predictions for a three-point bending isostatic beam introducing a threshold value $\mathcal{H}_c$ for the driving force term.

The stiffness matrix depends on the assumptions on material degradation, and the above two options are herein considered. In the bilateral degradation model, one has:

$$\mathbf{K}^* = \overline{E}_s \begin{bmatrix} \frac{A}{h_e} & 0 & 0 & -\frac{A}{h_e} & 0 & 0 \\ 0 & \frac{12I_x}{h_e^3} & \frac{6I_x}{h_e^2} & 0 & -\frac{12I_x}{h_e^3} & \frac{6I_x}{h_e^2} \\ 0 & \frac{6I_x}{h_e^2} & \frac{4I_x}{h_e} & 0 & -\frac{6I_x}{h_e^2} & \frac{2I_x}{h_e} \\ -\frac{A}{h_e} & 0 & 0 & \frac{A}{h_e} & 0 & 0 \\ -\frac{12I_x}{h_e^3} & -\frac{6I_x}{h_e^2} & 0 & \frac{12I_x}{h_e^3} & -\frac{6I_x}{h_e^2} & 0 \\ 0 & \frac{6I_x}{h_e^2} & \frac{2I_x}{h_e} & 0 & -\frac{6I_x}{h_e^2} & \frac{4I_x}{h_e} \end{bmatrix} \tag{37}$$

being $\overline{E}_s$ the effective elastic modulus of the damaged material, computed as:

$$\overline{E}_s = \frac{1}{h_e}\int_0^{h_e} E_s(z)\,\mathrm{d}z = \frac{1}{h_e}\sum_{i=1}^{2} E_0[(1-s(z^*))^2 + k_r] \tag{38}$$

where E_0 is the undamaged elastic modulus and a two-points Gaussian quadrature rule, which is sufficient to integrate exactly the integrand which is at most a quadratic function of z due to the above ansatz on the interpolation scheme for s, is used. The Gauss points' weights are unity and the coordinates are:

$$z^* = \frac{h_e}{2}\left[1 + (-1)^i \frac{\sqrt{3}}{3}\right], \quad i = 1, 2. \tag{39}$$

The scalar term $\mathcal{H}^e$ in the discretized setting entering $\boldsymbol{\mathcal{H}}^m$ and $\boldsymbol{\mathcal{H}}^v$ is also computed via numerical integration of the following expression:

$$\mathcal{H}^e = \frac{1}{h_e}\int_0^{h_e} \mathcal{H}\,\mathrm{d}z. \tag{40}$$

As previously outlined, in the staggered solution scheme, the vector $\mathbf{s}$ containing the nodal values of the phase field damage at nodes is frozen when solving the elastic problem. Therefore, the elastic equations become linear and a standard linear solver is used. When solving the phase field equations on a graph, $\mathcal{H}^e$ is frozen too, and again a linear solver is employed. Therefore, in the pseudo-algorithm 1, the computation of the neutral axis position at step 10 is done explicitly and the inner loop from step 9 to step 17 convergences in just one iteration.

In the monolateral damage degradation scheme, once $\overline{y}$ is determined, the effective bending stiffness is evaluated using the equations of a bi-material composite beam:

$$(EI_x)_s = E_0 I_x^{A_0} + E_0 A_0 d_0^2 + E_s I_x^{A_s} + E_s A_s d_s^2, \tag{41}$$

where

$$I_x^{A_0} = \frac{b}{12}\left(\frac{h}{2} + \overline{y}\right)^3, \tag{42a}$$

$$I_x^{A_s} = \frac{b}{12}\left(\frac{h}{2} - \overline{y}\right)^3, \tag{42b}$$

$$d_0 = \frac{1}{2}\left(\frac{h}{2} + \overline{y}\right), \tag{42c}$$

$$d_s = \frac{1}{2}\left(\frac{h}{2} - \overline{y}\right), \tag{42d}$$

and, for the axial stiffness:

$$(EA)_s = E_0 A_0 + E_s A_s. \tag{43}$$

Once E_s is computed at the element nodes, the same interpolation scheme and numerical integration used for calculating $\overline{E}_s$ in Eq. (38) is adopted to determine the effective values $\overline{EA}$ and $\overline{EI_x}$ accounting for the variability of s within the element. The final expression for the damaged stiffness matrix reads:

$$\mathbf{K}^* = \begin{bmatrix} \frac{(\overline{EA})}{h_e} & 0 & 0 & -\frac{(\overline{EA})}{h_e} & 0 & 0 \\ 0 & \frac{12(\overline{EI_x})}{h_e^3} & \frac{6(\overline{EI_x})}{h_e^2} & 0 & -\frac{12(\overline{EI_x})}{h_e^3} & \frac{6(\overline{EI_x})}{h_e^2} \\ 0 & \frac{6(\overline{EI_x})}{h_e^2} & \frac{4(\overline{EI_x})}{h_e} & 0 & -\frac{6(\overline{EI_x})}{h_e^2} & \frac{2(\overline{EI_x})}{h_e} \\ -\frac{(\overline{EA})}{h_e} & 0 & 0 & \frac{(\overline{EA})}{h_e} & 0 & 0 \\ -\frac{12(\overline{EI_x})}{h_e^3} & -\frac{6(\overline{EI_x})}{h_e^2} & 0 & \frac{12(\overline{EI_x})}{h_e^3} & -\frac{6(\overline{EI_x})}{h_e^2} & 0 \\ 0 & \frac{6(\overline{EI_x})}{h_e^2} & \frac{2(\overline{EI_x})}{h_e} & 0 & -\frac{6(\overline{EI_x})}{h_e^2} 0 & \frac{4(\overline{EI_x})}{h_e} \end{bmatrix}. \tag{44}$$

After solving for the displacement field, step 12 in Alg. 1, the characteristics of internal reactions are updated and convergence of the inner loop is assessed in terms of the displacement field at the step 17.

After convergence of the inner loop, the converged axial stress is calculated from the axial strain $\epsilon_z = \epsilon_0 + \chi_x y$, where ϵ_0 and χ_x are provided by the equations of equilibrium of the composite beam where the neutral axis position now is known:

$$\begin{bmatrix} M_{11} & M_{12} \\ M_{12} & M_{22} \end{bmatrix} \begin{bmatrix} \epsilon_0 \\ \chi_x \end{bmatrix} = \begin{bmatrix} N \\ M_x \end{bmatrix}. \tag{45}$$

The stress field solution is then used to compute the elastic strain energy of the element, step 20 in Alg. 1.

In analogy with implementations for the continuum [40], convergence of the staggered scheme is enforced by the satisfaction of the condition set in the step 23 of Alg. 1, which physically corresponds to a negligible variation of the internal damage state from an iteration to the next. The proposed algorithm has been implemented into MATLAB R2024.

Algorithm 1 Pseudo-code for the solution of the coupled problem for a given pseudo-time step t of a simulation, using a staggered scheme.

1: $k \leftarrow 1$ ▷ Staggered scheme iteration
2: $\mathbf{s}^k \leftarrow \mathbf{0}$
3: $E_e^k \leftarrow E_0$ $(\forall e \in \mathcal{E}_h)$
4: $M_x^i \leftarrow 0$, $N_x^i \leftarrow 0$ ▷ $\forall i \in \mathcal{V}_h$
5: set $\mathbf{F}^t$ ▷ Incremental loading path
6: DO ▷ Loop over k
7: $j \leftarrow 1$ ▷ Iteration of the nested nonlinear mech. problem
8: $M_x^i \leftarrow M_x^{i,k}$, $N^i \leftarrow N^{i,k}$ ▷ $\forall i \in \mathcal{V}_h$
9: DO ▷ Loop over j
10: find $\overline{y}^j$ ▷ $\forall i \in \mathcal{V}_h$
11: compute $\mathbf{K}^j$ based on $\mathbf{s}^k$ and $\overline{y}^j$
12: $\mathbf{U}^j = (\mathbf{K}^j)^{-1}\mathbf{F}^t$
13: compute updated $N^{i,j}$, $M_x^{i,j}$, $T_y^{i,j}$
14: $\mathbf{R}^j = \mathbf{U}^j - \mathbf{U}^{j-1}$
15: $j \leftarrow j + 1$
16: $N^i \leftarrow N^{i,j}$, $M_x^i \leftarrow M_x^{i,j}$, $T_y^i \leftarrow T_y^{i,j}$ ▷ $\forall i \in \mathcal{V}_h$
17: WHILE $\|\mathbf{R}^{j-1}\| < \mathrm{tol}_1$
18: compute $\boldsymbol{\epsilon}^k$
19: compute $\psi^k(\boldsymbol{\epsilon}^k, \mathbf{s}^k)$
20: compute $\mathcal{H}^m = \mathcal{H}^m(\psi^k)$, $\mathcal{H}^v = \mathcal{H}^v(\psi^k)$
21: $k \leftarrow k + 1$
22: solve $\mathbf{s}^k = (\mathcal{H}^m + l_0^2 \mathcal{L})^{-1} \mathcal{H}^v$
23: WHILE $\|\mathbf{s}^k - \mathbf{s}^{k-1}\| \leq \mathrm{tol}_2$

4. Application to a pioneering complex network material produced by 3D printing

The 3D printed complex network material recently manufactured and tested in compression in [29] is herein examined. Although the experimental data are not fully reported, it is considered a very relevant pioneering example of a possible network material

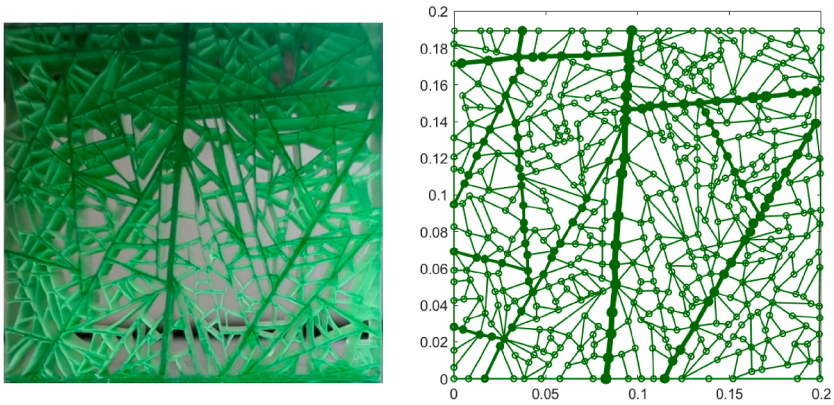

(a) 3D printed material [29] (b) Network model

Fig. 8. (a) Photo of a 3D printed complex network material (taken from a video shown by [29]), and (b) its network model.

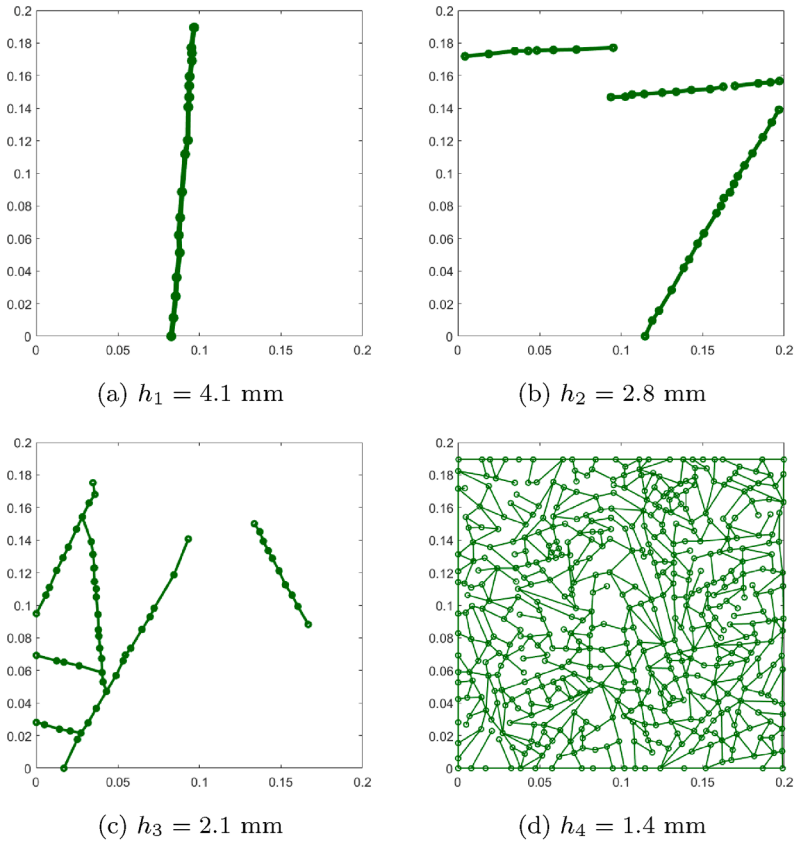

(a) $h_1 = 4.1$ mm (b) $h_2 = 2.8$ mm

(c) $h_3 = 2.1$ mm (d) $h_4 = 1.4$ mm

Fig. 9. Plot of edges composing the network according to the value of their height (from the thickest (a) to the thinnest (d)).

produced by 3D printing. It is made of edges having all the same base (the out-of-plane thickness of the 3D printed model) and variable heights and spans, see Fig. 8a. The reconstructed network model is shown in Fig. 8b.

Since the specimen size and the exact material properties are not available, a base of 200 mm and an out-of-plane thickness $b = 11.3$ mm have been set, for the purpose to provide a proof-of-concept simulation. This leads to four classes of edges according to the height of their cross-sections: the thickest edges have $h_1 = 4.1$ mm (Fig. 9a) and are sub-vertical, connecting the upper side of the specimen with the lower side. Edges with $h_2 = 2.8$ mm are further partitioning the domain and are shown in Fig. 9b, aligned sub-horizontally and one inclined. The left portion of the specimen is further partitioned by thinner straight edges with $h_3 = 2.1$ mm (Fig. 9c). Finally, all the other edges of the network with the thinnest height $h_4 = 1.4$ mm are randomly distributed in space (Fig. 9d).

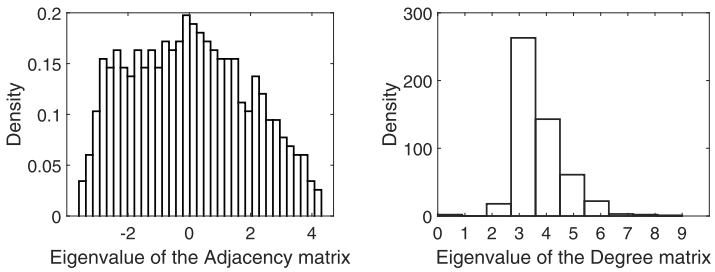

(a) Spectrum of the Adjacency matrix (b) Spectrum of the Degree matrix

Fig. 10. Properties of the graph related to the 3D printed material in terms of distribution density functions of the eigenvalues of the adjacency matrix (a) and of the degree matrix (b).

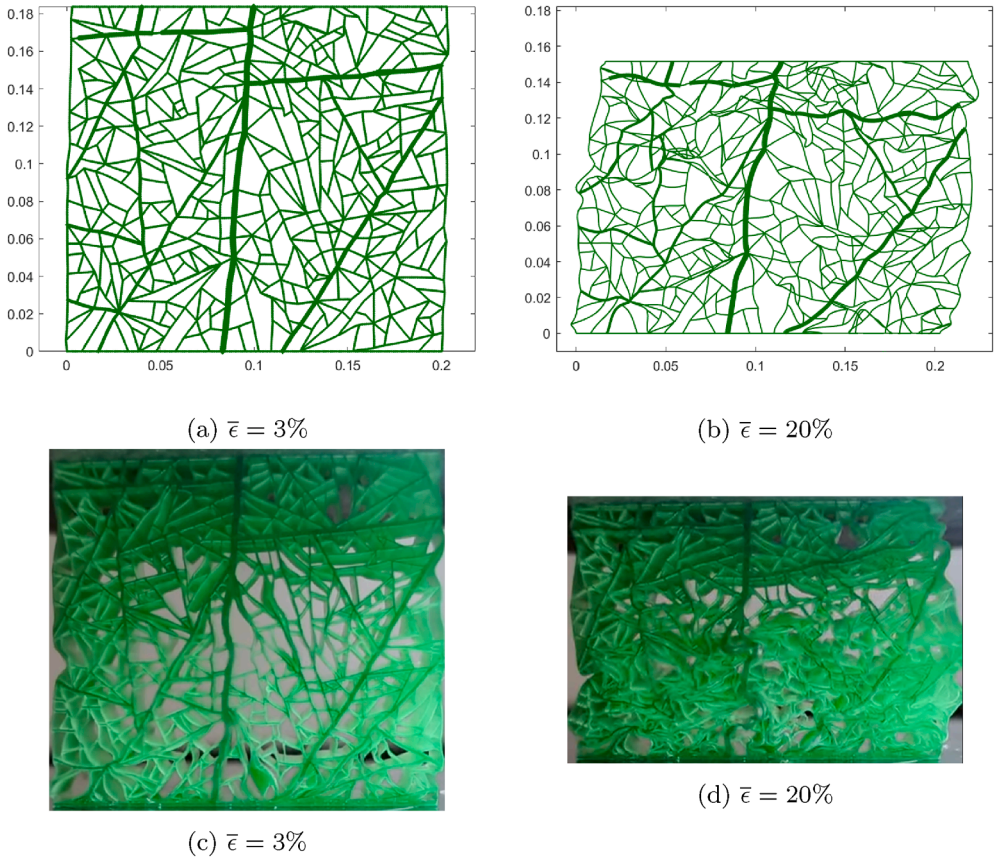

Fig. 11. Deformed meshes for two different applied compressive vertical displacements on the upper side of the model, leading to (a) 3 % apparent strain and (b) 20 % apparent strain. Simulations are qualitatively compared with experimental images from [29] in (c) and (d).

A previous investigation on the elastic interplay between randomly interconnected sub-networks with different stiffness was proposed in [62], but it was limited to two sub-networks.

The spectra of the adjacency matrix and of the degree matrix of the undirected graph associated to the complex material network are shown in Fig. 10. The probability density function of the eigenvalues of the adjacency matrix (Fig. 10a) are distributed according to a bell-shaped curve, similar to other types of biological networks [27]. The largest eigenvalue in Fig. 10a corresponds to the *average* degree of the network.

The spectrum of the degree matrix (Fig. 10b) consistently shows that the majority of vertices have 3 to 4 connections, but there are also few *hubs* with a larger number of connections ranging from 7 to 9, which are not so common in regular lattice materials. Bio-polymer random network models, for instance, feature a connectivity up to 4 [62,63]. To the best of author's knowledge, no studies explored a wider range of connectivities up to 9.

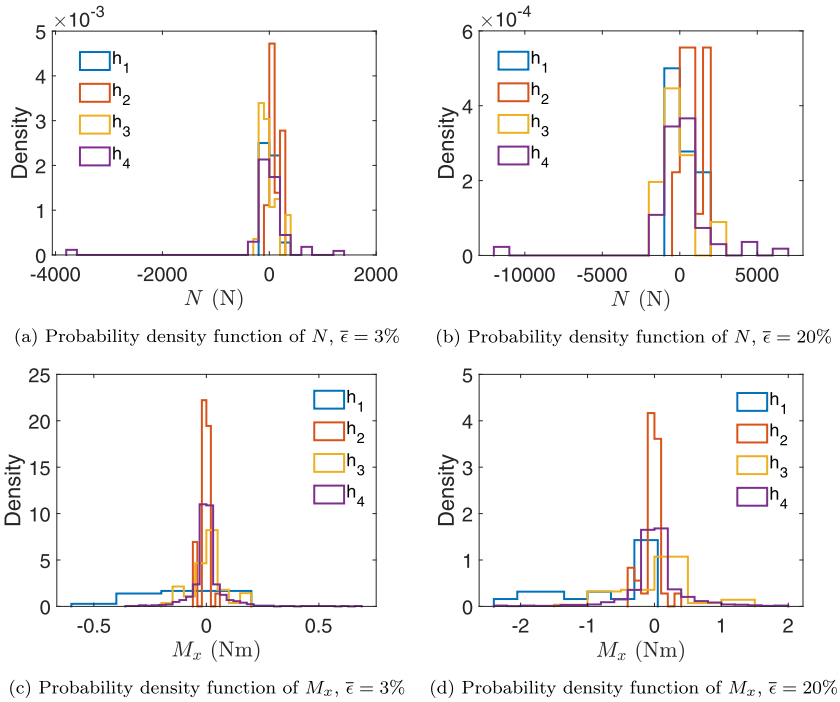

(a) Probability density function of N, $\bar{\epsilon} = 3\%$ (b) Probability density function of N, $\bar{\epsilon} = 20\%$

(c) Probability density function of M_x, $\bar{\epsilon} = 3\%$ (d) Probability density function of M_x, $\bar{\epsilon} = 20\%$

Fig. 12. Results of the numerical simulations in terms of distribution of axial forces and bending moments in the network.

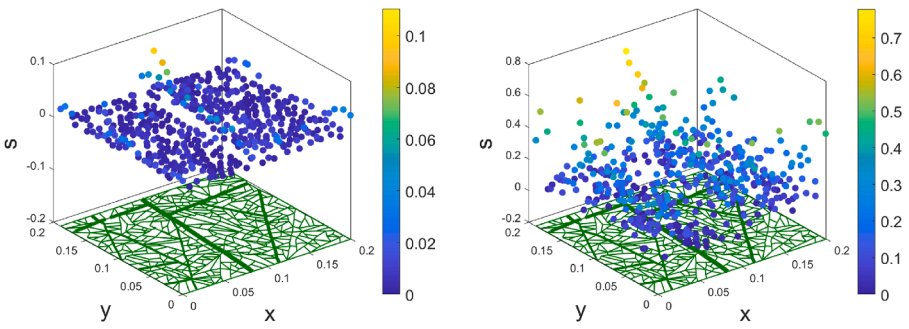

(a) Damage at graph vertices, $\bar{\epsilon} = 3\%$ (b) Damage at graph vertices, $\bar{\epsilon} = 20\%$

Fig. 13. Damage spread in the network subject to compression, for two different applied nominal vertical strain levels.

Other interesting network measures are the local and the global clustering coefficients, which are connected to percolation phenomena over the graph [64]. The local clustering coefficient of a vertex in a graph quantifies how close its neighbours are to being a clique, which is a subset of vertices in a graph where every pair of distinct vertices is connected by an edge (complete graph). The local clustering coefficient C_i for a vertex $\mathcal{V}_i$ is given by a proportion of the number of links between the vertices within its neighborhood, divided by the maximum number of links that could possibly exist between them. For an undirected graph, it can be expressed in terms of the adjacency matrix components as:

$$C_i = \frac{1}{k_i(k_i - 1)} \sum_{j,k} \mathcal{A}_{ij}\mathcal{A}_{jk}\mathcal{A}_{ki} \tag{46}$$

where $k_i = \sum_j \mathcal{A}_{ij}$ and $C_i = 0$ when k_i is zero or one. The average value of the local clustering coefficients of the graph provides a measure of the global clustering coefficient, which is the number of closed triplets over the total number of triplets of a graph. For the present complex network material, the global clustering coefficient C is equal to 0.11, which denotes low clustering and a critical percolation threshold scaling with $\propto 1/(C-1)$. This implies that diffusion-like phenomena, like damage, are expected to be relatively difficult to spread in the present material, which suggests it is a good candidate for mechanical applications.

Since the force-displacement curve is not available to perform a rigorous model parameter identification, the material properties were set to represent a plausible 3D printed material with an elastic modulus $E_0 = 2$ GPa, a fracture energy $G_c = 1$ N/m, and $l_0 = 1$ mm.

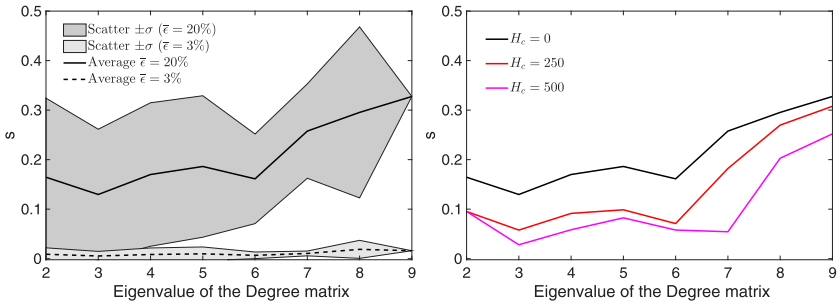

(a) Damage at graph vertices, $\bar{\epsilon} = 3\%$ (b) The effect of the threshold $\mathcal{H}_c$, $\bar{\epsilon} = 20\%$

Fig. 14. Correlation between average s and vertex degree for $\mathcal{H}_c = 0$: The shaded gray areas correspond to ± the standard deviation of the respective data. (a) $\bar{\epsilon} = 3\,\%$ (dashed curve), $\bar{\epsilon} = 20\,\%$ (solid curve). (b) The effect of the threshold $\mathcal{H}_c$ $(\mathrm{N/m})^2$ on the average damage as a function of the eigenvalue of the degree matrix.

The whole network consists of 515 vertices and 940 edges. For the application of the numerical method to avoid mesh dependency issues by complying with the requirement of the phase field formulation, a mesh size $h_e = l_0/2$ has been set for all the edges discretized with beam elements. This is achieved by inserting intermediate nodes between the edge vertices, equispaced by h_e. This led to 19,366 computational nodes with three degrees of freedom each and 19,790 finite elements for the mechanical problem. The set of algebraic equations for the mechanical problem consists of a sparse stiffness matrix of size 58098×58098. Accordingly, the graph Laplacian matrix has been projected onto this set of nodes, with resulting 19,366 linear algebraic equations.

The synthetic model of the network material is tested under uniaxial compression using the bilateral damage model to qualitatively replicate the observation made by [29]. Two imposed nominal axial deformation states of $\bar{\epsilon} = 3\,\%$ (Figs. 11a and 11c) and $\bar{\epsilon} = 20\,\%$ (Figs. 11b and 11d) are examined, representative of two extreme situations with low damage and high damage, respectively. The deformed shapes obtained by setting $\mathcal{H}_c = 0$ are qualitatively reproducing the deformation of the edges seen in the experiment, considering that the local instabilities taking place in the material network have not been included in the present simulations and are certainly important for high compressive strains.

To analyze the role played by the internal microstructures represented by edges with different orientation and height to partition the network domain, the probability distribution functions of the axial forces N and of the bending moments M_x are shown in Fig. 12 for the two values of $\bar{\epsilon}$. In terms of normal forces, all the distribution functions of the 4 sub-networks are well grouped in a small range of N (Fig. 12a), except few edges with the smallest height that are quite apart and are subject to very large compressive or tensile states. This trend persists also for a higher $\bar{\epsilon}$ (Fig. 12b).

On the other hand, the role of the sub-networks is quite different in terms of bending moments: thicker edges with height h_1 have a flatter distribution and are responsible for the extreme values of the internal bending moments acting on the network edges (Fig. 12c). Therefore, those edges have an important role in shading the other components from bending moments. The trend is further amplified for a higher $\bar{\epsilon}$ (Fig. 12d).

The value of the phase field damage at the vertices of the network is shown in Fig. 13 for $\bar{\epsilon} = 3\,\%$ and $20\,\%$, with the sketch of the network material displayed in green below. For $\bar{\epsilon} = 3\,\%$, damage is below 0.1 everywhere and accumulates primarily on the internal sub-structure of beams with the thickest height h_1, which shields the other components. This is due to the fact that it is the stiffer part of the network and it absorbs the majority of the load. For $\bar{\epsilon} = 20\,\%$, damage is reaching 0.8 and is much more spread over the entire network.

The correlation between the average level of damage in the graph vertices and their degree of connection is shown in Fig. 14a, for the two applied strain levels. The spread of data is shown with gray areas corresponding to ± the standard deviation around the curves denoting the average values. The results related to this network material suggest that damage is increasing with the number of connections of the node. Further quantitative investigations are required to better assess the role of the sub-network properties with respect to the degree of connectivity of the network nodes, to draw more general conclusions on the performance of these materials. The effect of introducing a threshold $\mathcal{H}_c$ different from zero is analyzed in Fig. 14b, where we appreciate a progressive reduction of damage in the vertices as a function of $\mathcal{H}_c$, in a nonlinear way.

5. Conclusion and research perspectives

This work proposed a new theory for the simulation of nonlocal damage in a 2D lattice structure made of polymeric materials and discretized by Euler-Bernoulli beam finite elements. Damage is modelled according to a phase field formulation that has been suitably projected onto the discretized set of nodes and elements through the graph Laplacian matrix, which has been exploited for the very first time to treat a Helmoltz differential equation associated to phase field damage evolution.

Coupling of phase field evolution equation with mechanics has been done according to two possible damage scenarios: the former assumed bilateral damage applied to the Young's modulus in tension and in compression, while the latter introduced a monolateral damage affecting the Young's modulus of the material only in tension. Both formulations have been compared with results from experimental bending tests on ABS material that show damage evolution due to progressive polymer crazing. Both formulations

allowed simulating a damage scenario where the variable damage s is comprised between zero and unity, and differed from previous approaches for the simulation of brittle crack growth [53,54] where the phase field is either zero o unity along the cross-section depth. Moreover, the additional enhancement of the formulations by the introduction of a threshold driving force $\mathcal{H}_c$ allowed to achieve a better prediction of the onset of damage, and offered a way to apply the bilateral damage formulation with different values of $\mathcal{H}_c$ to make lower and upper bound predictions to the mechanical response. This is particularly useful for parametric analyses, since the bilateral damage formulation allows preserving the linearity of the mechanical problem in each staggered iteration, while the monolateral damage does not and is therefore computationally more demanding.

According to the proposed staggered scheme, where alternate minimization of the two differential problems is carried out, the algorithm foresees the computation of the elastic solution for a frozen damage state and the computation of a driving force to be passed in input to the phase field evolution equations related to the elastic energy of the system in each node.

The potentiality of the new methodology has been tested in relation to a preliminar realization of a complex network material produced by 3D printing and taken from the literature. The non availability of a complete experimental characterization did not allow to perform quantitative comparisons, but the problem has been addressed as a proof-of-concept to show the applicability of the proposed method to such complex materials which have topological features distinct from those of physical networks. It has been shown that the model is able to extract quantitative information on axial and bending moments distributions in the beams composing the network and put in connection damage to the degree of connectivity of the nodes, which are intrinsically linked in the phase field evolution equation projected onto a graph, as demonstrated in this study. Said that, more systematic investigations are necessary to better understand the interplay between the different sub-network stiffness and the nodal degree of connectivity, and expand the study by considering multiple realizations of random networks.

In this regard, the proposed model enables systematic analyses that, in parallel with progresses done by theoretical and experimental physicists, may lead soon to quantitative results on new types of metamaterials in a nonlinear regime, made by 3D printing and with such complex internal structures. The 3D printed technology is opening new perspectives for manufacturing [65], and there is a urgent need to analyze those new materials also in terms of reliability and damage [66] in addition to their wave propagation properties, and extend the applications to random microstructures which appear to have a higher toughness as compared to periodic ones [67].

While these open issues should be systematically investigated in dedicated follow-up articles, it is believed that the present proof-of-concept results show that the proposed model enables performing nonlinear analyses on large scale samples, exploiting the advantage of the bilateral damage model enhanced by suitable threshold values to speed up simulations, and eventually allow gathering results related to multiple network realizations in an unprecedented efficient way.

CRediT authorship contribution statement

Marco Paggi : Writing – review & editing, Writing – original draft, Visualization, Validation, Software, Resources, Project administration, Methodology, Investigation, Funding acquisition, Formal analysis, Data curation, Conceptualization.

Data availability

Data will be made available on request. Benchmark codes and updated releases on the project of mechanics for network materials are provided on GitHub: https://github.com/marcopaggi/mech4netmat.git

Declaration of competing interest

The author declares that he has no known competing financial interests or personal relationships that could have appeared to influence the work reported in this paper.

References

[1] V.S. Deshpande, N.A. Fleck, M.F. Ashby, Effective properties of the octet-truss lattice material, J. Mech. Phys. Solids 49 (8) (2001) 1747–1769.
[2] V.S. Deshpande, M.F. Ashby, N.A. Fleck, Foam topology: bending versus stretching dominated architectures, Acta Mater. 49 (6) (2001) 1035–1040.
[3] V. Deshpande, N.A. Fleck, Collapse of truss core sandwich beams in 3-point bending, Int. J. Solids Struct. 38 (36) (2001) 6275–6305.
[4] S.N. Khaderi, V.S. Deshpande, N.A. Fleck, The stiffness and strength of the gyroid lattice, Int. J. Solids Struct. 51 (23) (2014) 3866–3877.
[5] C. Tang, Y. Xu, K. Zhou, Y. Xie, Y. Ma, C. Li, F. Xu, H. Zhou, B. Xu, Mechanism behind the deterioration in gel properties of collagen gel induced by high-temperature treatments: a molecular perspective, Food Res. Int. 171 (2023) 112985.
[6] S. Riedel, P. Hietschold, C. Krömmelbein, T. Kunschmann, R. Konieczny, W. Knolle, C.T. Mierke, M. Zink, S.G. Mayr, Design of biomimetic collagen matrices by reagent-free electron beam induced crosslinking: structure-property relationships and cellular response, Mater. Des. 168 (2019) 107606.
[7] M. Hadjiargyrou, Incorporation of dna into electrospun nanofibrous scaffolds: Fundamental characterization studies and gene delivery, 18, IntechOpen, Rijeka, 2011.
[8] M. Jaspers, S.L. Vaessen, P.V. Schayik, D. Voerman, A.E. Rowan, P.H.J. Kouwer, Nonlinear mechanics of hybrid polymer networks that mimic the complex mechanical environment of cells, Nat. Commun. 8 (2017) 15478.
[9] G.A. Holzapfel, R.W. Ogden, An arterial constitutive model accounting for collagen content and cross-linking, J. Mech. Phys. Solids 136 (2020) 103682.
[10] R.C. Picu, Mechanics of random fiber networks-a review, Soft Matter 7 (2011) 6768–6785.
[11] M. Fallah, H. Zarei, M. Paggi, A novel in-situ micro-mechanical testing of paper fracture and its stochastic network model, 2024, p. 112930.
[12] K.A. Jansen, A.J. Licup, A. Sharma, R. Rens, F.C. Mackintosh, G.H. Koenderink, The role of network architecture in collagen mechanics, Biophys. J. 114 (11) (2018) 2665–2678.
[13] C. Aermes, A. Hayn, T. Fischer, C.T. Mierke, Environmentally controlled magnetic nano-tweezer for living cells and extracellular matrices, Sci. Rep. 10 (2020) 13453.

[14] C.P. Broedersz, X. Mao, T.C. Lubensky, F.C. Mackintosh, Criticality and isostaticity in fibre networks, Nat. Phys. 7 (2011) 983–988.
[15] A. Sharma, A.J. Licup, K.A. Jansen, R. Rens, M. Sheinman, G.H. Koenderink, F.C. Mackintosh, Strain-controlled criticality governs the nonlinear mechanics of fibre networks, Nat. Phys. 12 (2016) 584–587.
[16] P.R. Onck, T. Koeman, T.V. Dillen, E.V.D. Giessen, Alternative explanation of stiffening in cross-linked semiflexible networks, Phys. Rev. Lett. 95 (2005) 178102.
[17] S.B. Lindström, D.A. Vader, A. Kulachenko, D.A. Weitz, Biopolymer network geometries: characterization, regeneration, and elastic properties, Phys. Rev. E 82 (2010) 51905.
[18] A.S. Shahsavari, R.C. Picu, Exceptional stiffening in composite fiber networks, Phys. Rev. E 92 (2015) 12401.
[19] J.M.V. Doorn, L. Lageschaar, J. Sprakel, J.V.D. Gucht, Criticality and mechanical enhancement in composite fiber networks, Phys. Rev. E 95 (2017) 42503.
[20] D.J. Watts, S.H. Strogatz, Collective dynamics of 'small-world' networks, Nature 393 (1998) 440–442.
[21] A.-L. Barabási, A. Réka, Emerging of scaling in random networks, Science 286 (1999) 509–512.
[22] R. Albert, A.L. Barabasi, Statistical mechanics of complex networks, Rev. Mod. Phys. 74 (2002) 47–97.
[23] W. Hoppitt, N.J. Boogert, K.N. Laland, Detecting social transmission in networks, J. Theor. Biol. 263 (2010) 544–555.
[24] M. Bardoscia, P. Barucca, S. Battiston, F. Caccioli, G. Cimini, D. Garlaschelli, F. Saracco, T. Squartini, G. Caldarelli, The physics of financial networks, Nature Rev. Phys. 3 (2021) 490–507.
[25] N. Dehmamy, S. Milanlouei, A.-L. Barabási, A structural transition in physical networks, Nature 563 (2018) 676–680.
[26] Y. Liu, N. Dehmamy, A.-L. Barabási, Isotopy and energy of physical networks, Nat. Phys. 17 (2021) 216–222.
[27] M. Pósfai, B. Szegedy, I. Bačić, L. Blagojević, M. Abért, J. Kertész, L. Lovász, A.-L. Barabási, Impact of physicality on network structure, Nat. Phys. 20 (2024) 142–149.
[28] C. Glover, A.-L. Barabási, Measuring entanglement in physical networks, Phys. Rev. Lett. 133 (2024) 77401.
[29] A.-L. Barabási, From physical network to network materials, in: APS Global Physics Summit, Anaheim, CA, 2025.
[30] G. Pijaudier-Cabot, Z.P. Bažant, Nonlocal damage theory, J. Eng. Mech. 113 (1987) 1512–1533.
[31] Z.P. Bažant, M. Jirásek, Nonlocal integral formulations of plasticity and damage: survey of progress, J. Eng. Mech. 128 (2002) 1119–1149.
[32] R.H.J. Peerlings, R.D. Borst, W.A.M. Brekelmans, J.H. P.D. Vree, Gradient-enhanced damage for quasi-brittle materials, Int. J. Numer. Methods Eng. 39 (1996) 3391–3403.
[33] M. Jirásek, Nonlocal models for damage and fracture: comparison of approaches, Int. J. Solids Struct. 35 (1998) 4133–4145.
[34] M. Jirásek, S. Rolshoven, Comparison of integral-type nonlocal plasticity models for strain-softening materials, Int. J. Eng. Sci. 41 (2003) 1553–1602.
[35] E. Lorentz, V. Godard, Gradient damage models: toward full-scale computations, Comput. Methods Appl. Mech. Eng. 200 (1927).
[36] G.A. Francfort, J.-J. Marigo, Revisiting brittle fracture as an energy minimization problem, J. Mech. Phys. Solids 46 (8) (1998) 1319–1342.
[37] B. Bourdin, G.A. Francfort, J.-J. Marigo, Numerical experiments in revisited brittle fracture, J. Mech. Phys. Solids 48 (2000) 797–826.
[38] L. Ambrosio, Existence theory for a new class of variational problems, Arch. Ration. Mech. Anal. 111 (4) (1990) 291–322.
[39] E. Tanné, T. Li, B. Bourdin, J.-J. Marigo, C. Maurini, Crack nucleation in variational phase-field models of brittle fracture, J. Mech. Phys. Solids 110 (2018) 80–99.
[40] R. Cavuoto, P. Lenarda, D. Misseroni, M. Paggi, D. Bigoni, Failure through crack propagation in components with holes and notches: an experimental assessment of the phase field model, Int J Solids Struct 257 (2022) 111798.
[41] R. Cavuoto, P. Lenarda, A. Tampieri, D. Bigoni, M. Paggi, Phase-field modelling of failure in ceramics with multiscale porosity, Mater. Des. 238 (2024) 112708.
[42] M. Frémond, B. Nedjar, Damage, gradient of damage and principle of virtual power, Int. J. Solids Struct. 33 (8) (1996) 1083–1103.
[43] C. Miehe, M. Hofacker, F. Welschinger, A phase field model for rate-independent crack propagation: robust algorithmic implementation based on operator splits, Comput. Methods Appl. Mech. Eng. 199 (45) (2010) 2765–2778.
[44] H. Amor, J.-J. Marigo, C. Maurini, Regularized formulation of the variational brittle fracture with unilateral contact: numerical experiments, J. Mech. Phys. Solids 57 (8) (2009) 1209–1229.
[45] F. Freddi, G. Royer-Carfagni, Regularized variational theories of fracture: a unified approach, J. Mech. Phys. Solids 58 (2010) 1154–1174.
[46] F. Freddi, G. Royer-Carfagni, Variational fracture mechanics to model compressive splitting of masonry-like materials, Ann. Solid Struct. Mech. 2 (2011) 57–67.
[47] J.-Y. Wu, A unified phase-field theory for the mechanics of damage and quasi-brittle failure, J. Mech. Phys. Solids 103 (2017) 72–99.
[48] M. Ambati, T. Gerasimov, L.D. Lorenzis, A review on phase-field models of brittle fracture and a new fast hybrid formulation, Comput. Mech. 55 (2015) 383–405.
[49] M. Ambati, T. Gerasimov, L.D. Lorenzis, Phase-field modeling of ductile fracture, Comput. Mech. 55 (2015) 1017–1040.
[50] F. Freddi, G. Royer-Carfagni, Phase-field slip-line theory of plasticity, J. Mech. Phys. Solids 94 (2016) 257–272.
[51] J. Kiendl, M. Ambati, L.D. Lorenzis, H. Gomez, A. Reali, Phase-field description of brittle fracture in plates and shells, Comput. Methods Appl. Mech. Eng. 312 (2016) 374–394.
[52] J. Reinoso, M. Paggi, C. Linder, Phase field modeling of brittle fracture for enhanced assumed strain shells at large deformations: formulation and finite element implementation, Comput. Mech. 59 (2017) 981–1001.
[53] W. Lai, J. Gao, Y. Li, M. Arroyo, Y. Shen, Phase field modeling of brittle fracture in an euler-bernoulli beam accounting for transverse part-through cracks, Comput. Methods Appl. Mech. Engrg. 361 (2020) 112787.
[54] P. Xu, Y. Zhang, H. Jia, F. Cheng, A mixed-element phase field method for the fracture analysis of beams, Eng. Fract. Mech. 307 (2024) 110316.
[55] F. Chung, Spectral Graph Theory, American Mathematical Society, 1988.
[56] K.-J. Bathe, Finite Element Procedures, Prentice Hall, 1996.
[57] T. Gerasimov, U. Römer, J. Vondrejc, H.G. Matthies, L.D. Lorenzis, Stochastic phase-field modeling of brittle fracture: computing multiple crack patterns and their probabilities, Comput. Methods Appl. Mech. Engrg. 372 (2020) 113353.
[58] M. Paggi, J. Reinoso, An anisotropic large displacement cohesive zone model for fibrillar and crazing interfaces, Int. J. Solids Struct. 69 (2015) 106–120.
[59] K.M. Conway, G.J. Pataky, Crazing in additively manufactured acrylonitrile butadiene styrene, Eng. Fract. Mech. 211 (2019) 114–124.
[60] Z. Wang, K. Zhou, C. Bi, Exploring flexural performances of fused filament fabrication -printed and -composites through innovative bio-inspired processing parameter optimization, Appl. Compos. Mater. 31 (2024) 929–958.
[61] M.A. Dundar, G.S. Dhaliwal, E. Ayorinde, M. Al-Zubi, Tensile, compression, and flexural characteristics of acrylonitrile-butadiene-styrene at low strain rates: experimental and numerical investigation, Polym. Polym. Compos. 29 (2021) 331–342.
[62] E. Lerner, E. Bouchbinder, Scaling theory of critical strain-stiffening in disordered elastic networks, Extreme Mech. Lett. 65 (2023) 102104.
[63] S. Kakaletsis, E. Lejeune, M. Rausch, The mechanics of embedded fiber networks, J. Mech. Phys. Solids 181 (2023) 105456.
[64] B. Bollobás, O. Riordan, Sharp thresholds and percolation in the plane, Random Struct. Algorithm. 29 (2006) 534–548.
[65] A.S. Meeussen, A. Corvi, K. Bertoldi, A new design strategy for highly multistable kirigami metamaterials, 2025, p. 2421638.
[66] Y. Zheng, W. Qiu, X. Liu, Z. Huang, L. Xia, Damage-tolerant mechanical metamaterials designed by fail-safe topology optimization, Mater. Des. 249 (2025) 113546.
[67] S. Fulco, M.K. Budzik, H. Xiao, D.J. Durian, K.T. Turner, Disorder enhances the fracture toughness of 2d mechanical metamaterials, PNAS Nexus 4 (2) (2025) 23.